

Supplementary Materials

Suppressing Defects Through Synergistic Effect of Lewis Base and Lewis Acid for Highly Efficient and Stable Perovskite Solar Cells

Fei Zhang,^{1,2} Dongqin Bi,² Norman Pellet,² Chuanxiao Xiao,¹ Zhen Li,¹ Joseph J. Berry,¹ Shaik Mohammed Zakeeruddin,² Kai Zhu,^{1,*} Michael Grätzel^{2,*}

¹ National Renewable Energy Laboratory, Golden, Colorado 80401, USA

² Laboratory of Photonics and Interfaces, Institute of Chemical Sciences and Engineering, École Polytechnique Fédérale de Lausanne (EPFL), Station 6 CH-1015, Lausanne, Switzerland

Correspondence and requests for materials should be addressed to K.Z. (email: kai.zhu@nrel.gov) or to M.G. (email: michael.gratzel@epfl.ch)

Experimental

Materials: All solution chemicals were purchased from Acros and used as-received without any other refinement unless otherwise specified. 30NRT TiO₂ paste, MABr, and FAI were purchased from Greatcell Solar. N-(4-bromophenyl)thiourea, PbI₂, and PbBr₂ were from TCI Corporation. Spiro-OMeTAD was received from Merck Corporation. The bis-PCBM, titanium diisopropoxide bis(acetylacetonate), bis(trifluoromethanesulfonyl)imide lithium salt, and tert-butylpyridine were purchased from Sigma-Aldrich.

Instrument and Measurements: SEM (FEI Nova 630, field-emission gun) imaging was performed with an electron-beam voltage of 3 kV and current of 3 nA in the immersion-lense mode. Photoluminescence (PL) spectra were recorded with a Fluorolog-Horiba fluorometer. The XRD patterns were acquired with a Bruker D8 Discover diffractometer in Bragg–Brentano mode, using Cu K α radiation (1.540598 Å) and a Ni β -filter. Spectra were acquired with a linear silicon strip “Lynx Eye” detector from 2 θ = 10°–60° at a scan rate of 2° min⁻¹, step width of 0.02°, and a source slit width of 1 mm. A baseline correction was applied to all X-ray thin-film diffractograms to compensate for the broad feature arising from the glass.

Device Fabrication: Devices were prepared on conductive fluorine-doped tin oxide (FTO)-coated glass substrates. The substrates were cleaned extensively by deionized water, acetone, and isopropanol. A compact titanium dioxide (TiO₂) layer of about 40 nm was deposited by spray pyrolysis of 7 mL 2-propanol solution containing 0.6 mL titanium diisopropoxide bis(acetylacetonate) solution (75% in 2-propanol, Sigma-Aldrich) and 0.4 mL acetylacetone

at 450°C in air. On top of this layer, mesoporous titanium dioxide was formed by spin-coating 30-nm-sized nanoparticles (Dyesol 30NRD, Dyesol) diluted in ethanol (1:6 w/w) at 4,500 rpm for 15 s. The [(FAI)_{0.81}(PbI₂)_{0.85}(MABr)_{0.15}(PbBr₂)_{0.15}] precursor solution was prepared in a glovebox from a 1.35M Pb²⁺(PbI₂ and PbBr₂) and 0.6 mg/mL BrPh-ThR in the mixed solvent of DMF and DMSO; the volume ratio of DMF/DMSO is 4:1. The spin-coating procedure was performed by 2,000 rpm for 10 s followed with 6,000 rpm for 30 s. At 15 s before the last spin-coating step, 110 mL of bis-PCBM solution with 0.8 mg/mL from chlorobenzene was pipetted onto the substrate. Thereafter, the substrate was put onto a hotplate for 1 hour at 100°C. Subsequently, the hole-transporting layer (HTM) was deposited on the top of the perovskite by spin coating at 4,000 rpm for 15 s. The spiro-OMeTAD solutions were prepared dissolving the spiro-OMeTAD in 1 mL chlorobenzene at a concentration of 60 mM, with the addition of 30 mM bis(trifluoromethanesulfonyl)imide lithium salt from a stock solution in acetonitrile, 200 mM of tert-butylpyridine. The devices were finalized by thermal evaporation of 80 nm gold.

J-V Characterization: The J-V characteristics of the devices were measured under 100 mW/cm² conditions using a 450 W xenon lamp (Oriel) as a light source, equipped with a Schott K113 Tempax sunlight filter (Praezisions Glas & Optik GmbH) to match the emission spectra to the AM1.5G standard in the region of 350–750 nm. The current–voltage characteristics of the devices were obtained by applying external potential bias to the cell while recording the generated photocurrent using a Keithley (Model 2400) digital source meter. The J–V curves of all devices were measured by masking the active area with a metal mask of area 0.16 cm².

IPCE: The incident photon to current conversion efficiency of the devices was measured by focusing light from the 300 W xenon lamp (ILC Technology, U.S.A.) through a Gemini-180 double monochromator (Jobin Yvon Ltd., U.K.). The monochromatic light was chopped at 3 Hz before impinging onto the photovoltaic cell. The monochromator was incremented through the visible spectrum to generate the IPCE dependence on wavelength.

Hall Effect Measurements: Hall effect measurements were carried out with Ecopia HMS 3000 setup (Microworld) with a magnetic field of 0.54 T in a 4-point configuration measuring an area of 1 cm². The perovskite layer was deposited on microscope glass with the same method of how we prepared for solar cells and contacted via Au by thermal evaporation (200 nm). The thickness of the perovskite films was measured by a profiler (Tencor Alpha step 500).

C-AFM measurements: C-AFM results were collected by a Veeco D5000 AFM system in a glovebox equipped with the Nanoscope V controller. A nanosensor PPP-EFM tip was

employed in the contact mode for the AFM scan. A bias voltage of 1 V was applied to the sample, with the tip virtually grounded. The scan area is $2 \times 2 \mu\text{m}$ with 1,024 points on the fast axis and 256 lines on the slow axis; the scan rate is 0.2 Hz/line. All results were acquired via the same tip; the measurements were performed on at least two locations and the results are similar. After the scans on all samples, we re-scan the first sample to confirm that there is no change of the AFM tip.

Long-Term Light-Soaking Test: Stability measurements were performed with a Biologic MPG2 potentiostat under a full AM1.5 sun-equivalent white LED lamp. The devices were measured with a maximum power-point (MPP) tracking routine under continuous illumination (and nitrogen). The MPP was updated every 10 s by a standard perturb-and-observe method. Every 1 minute a JV curve was recorded to track the evolution of individual JV parameters.

PL Decay Analysis: Neglecting Auger-type recombination, we analyze the kinetics of the PL decay by the differential rate law:

$$-\frac{dn}{dt} = k_1 n + k_2 n^2, \quad (\text{S1})$$

where k_1 and k_2 are the first- and second-order rate constants for non-radiative (trap-controlled) and bimolecular radiative recombination of the photo-generated charge carriers, and n is the charge-carrier concentration, respectively.³³ Given that the perovskite is not doped, showing only weak p-conduction in the pristine state, we assume that most charge carriers are photo-generated; hence, the electrons and holes are present at equal concentration throughout the reaction ($n_{e^-} = n_{h^+} = n$). Integration of Eq. S1 yields Eq. S2, where n^0 and $n(t)$ denote the concentration of charge carriers immediately after laser excitation of the perovskite and at time t , respectively:

$$n(t) = \frac{k_1}{k_2} \cdot \frac{1}{e^{k_1 t} \cdot \left(1 + \frac{k_1}{n^0 k_2}\right) - 1}. \quad (\text{S2})$$

The temporal decay of the photoluminescence intensity $I_{\text{PL}}(t)$ is shown in Figure 2b, reflecting the number of photons emitted by the perovskite per unit time. As the photons are

generated by bimolecular radiative recombination of charge carriers, their concentration (n_{hv}) varies according to the differential rate law:

$$I_{PL}(t) \sim \frac{dn_{hv}}{dt} = k_2 n^2 = \frac{k_1^2}{k_2} \cdot \frac{1}{\left[e^{k_1 t} \cdot \left(1 + \frac{k_1}{n^0 k_2} \right) - 1 \right]^2} \quad (\text{S3})$$

The dashed lines plotted in **Figure S3** reflect the decay kinetics described by Eq. **S3**. Their excellent fit with all four of the experimental curves validates the kinetic model that we applied to interpret the PL data.

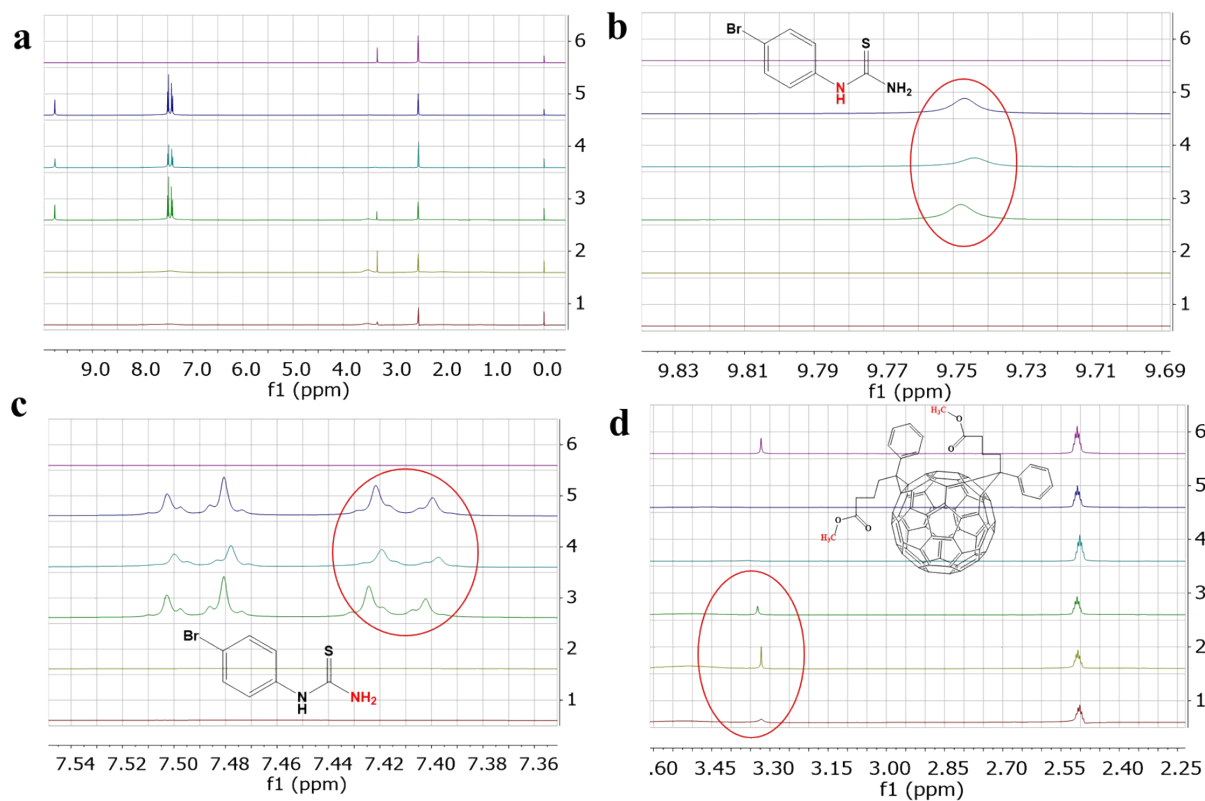


Figure S1 ^1H NMR of corresponding samples in solution (1) bis-PCBM; (2) bis-PCBM + PbI_2 ; (3) bis-PCBM + BrPh-ThR + PbI_2 ; (4) BrPh-ThR; (5) BrPh-ThR + PbI_2 ; (6) PbI_2 .

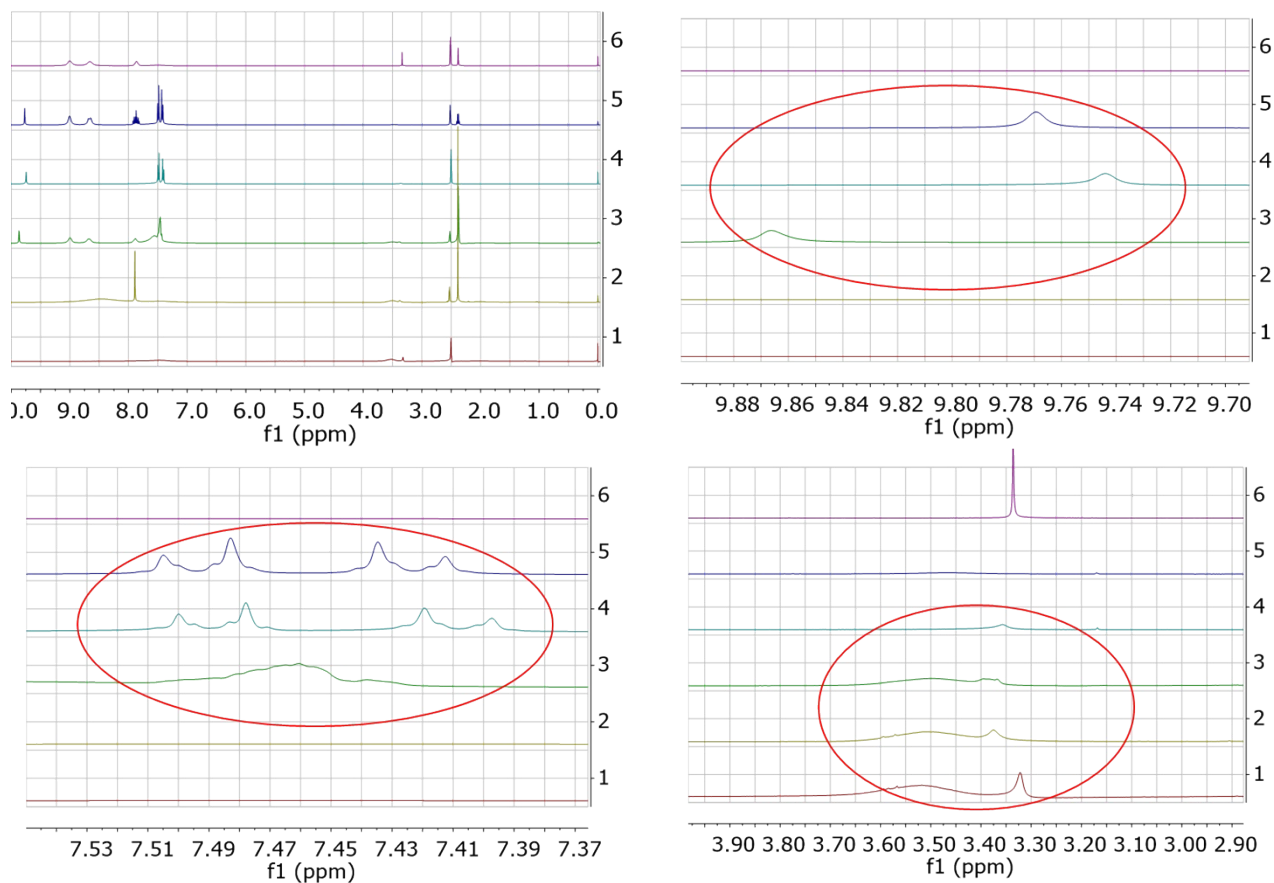


Figure S2 ^1H NMR of corresponding samples in solution (1) bis-PCBM; (2) bis-PCBM + $[(\text{FAI})_{0.81}(\text{PbI}_2)_{0.85}(\text{MABr})_{0.15}(\text{PbBr}_2)_{0.15}]$; (3) bis-PCBM + BrPh-ThR + $[(\text{FAI})_{0.81}(\text{PbI}_2)_{0.85}(\text{MABr})_{0.15}(\text{PbBr}_2)_{0.15}]$; (4) BrPh-ThR; (5) BrPh-ThR + $[(\text{FAI})_{0.81}(\text{PbI}_2)_{0.85}(\text{MABr})_{0.15}(\text{PbBr}_2)_{0.15}]$; (6) $[(\text{FAI})_{0.81}(\text{PbI}_2)_{0.85}(\text{MABr})_{0.15}(\text{PbBr}_2)_{0.15}]$.

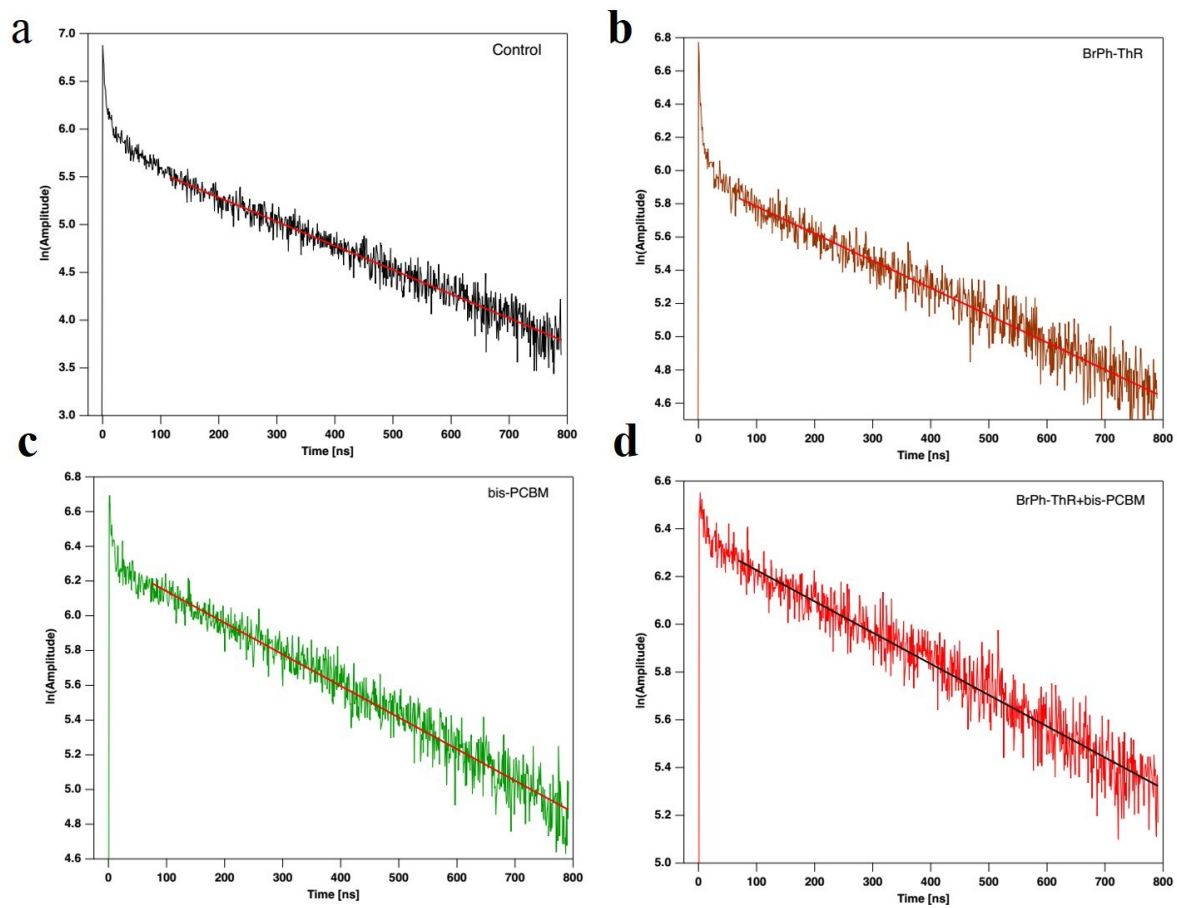


Figure S3 Linear fits of the TRPL curves of corresponding samples.

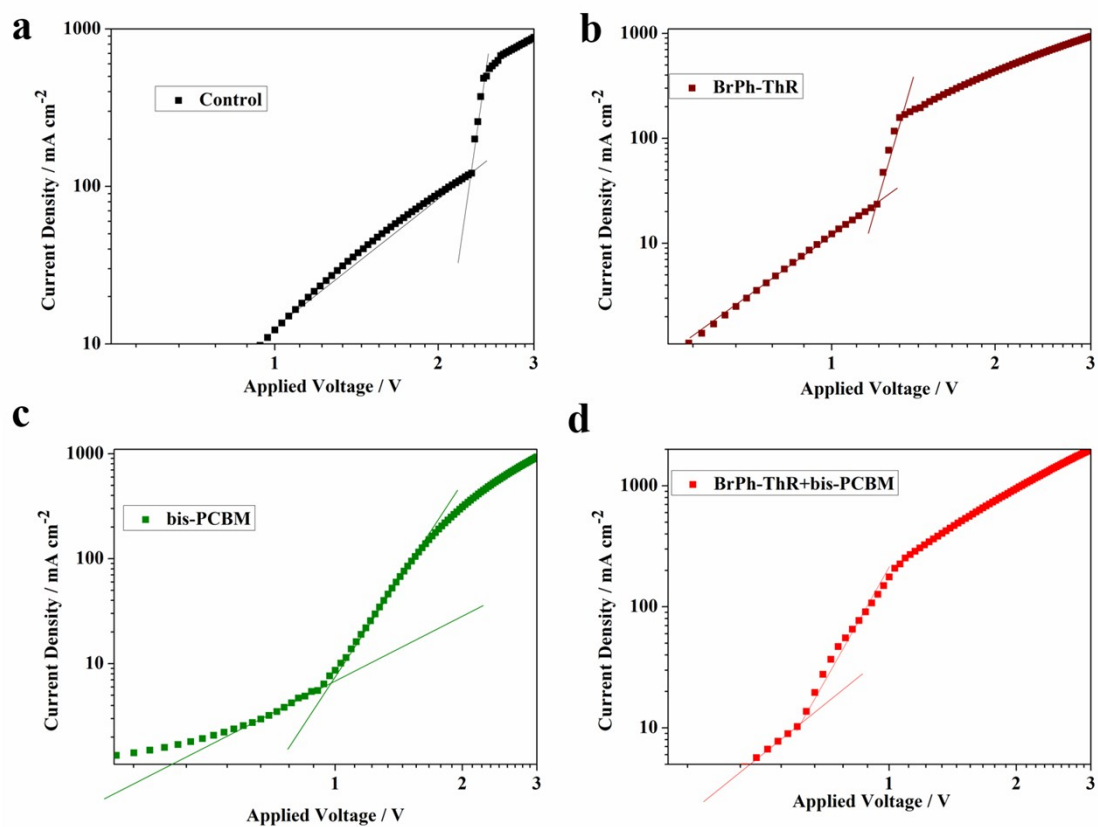


Figure S4 J–V curves of corresponding devices with a structure of ITO / PEDOT:PSS / perovskite / MoO₃ / Au.

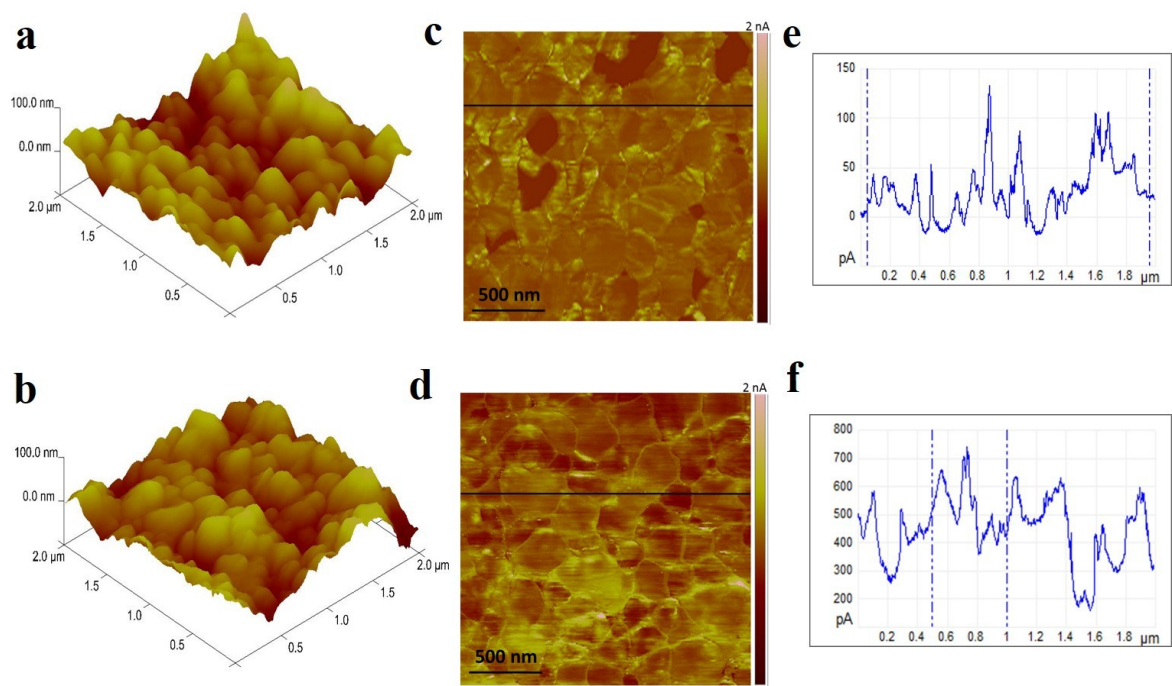


Figure S5 The AFM morphology ($2 \times 2 \mu\text{m}$) of perovskite films (a) control; (b) with bis-PCBM+BrPh-ThR. C-AFM images for the perovskite films (c,e) control; (d,f) with bis-PCBM+BrPh-ThR obtained at a bias voltage of 1 V in the dark.

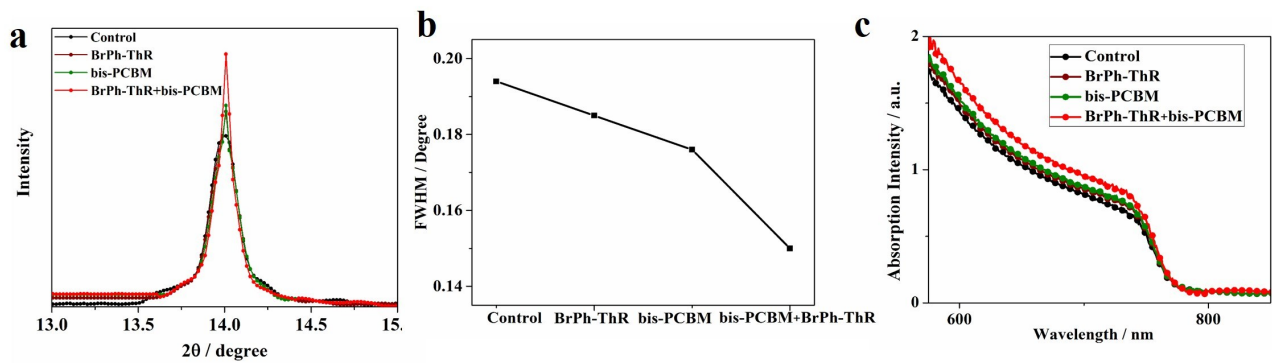


Figure S6 (a) XRD patterns from 13.0 to 15.0 degree of corresponding films on meso-TiO₂ / compact TiO₂ / FTO substrate; (b) the FWHM of the (110) peak of corresponding XRD patterns; (c) the absorption spectra of the corresponding films.

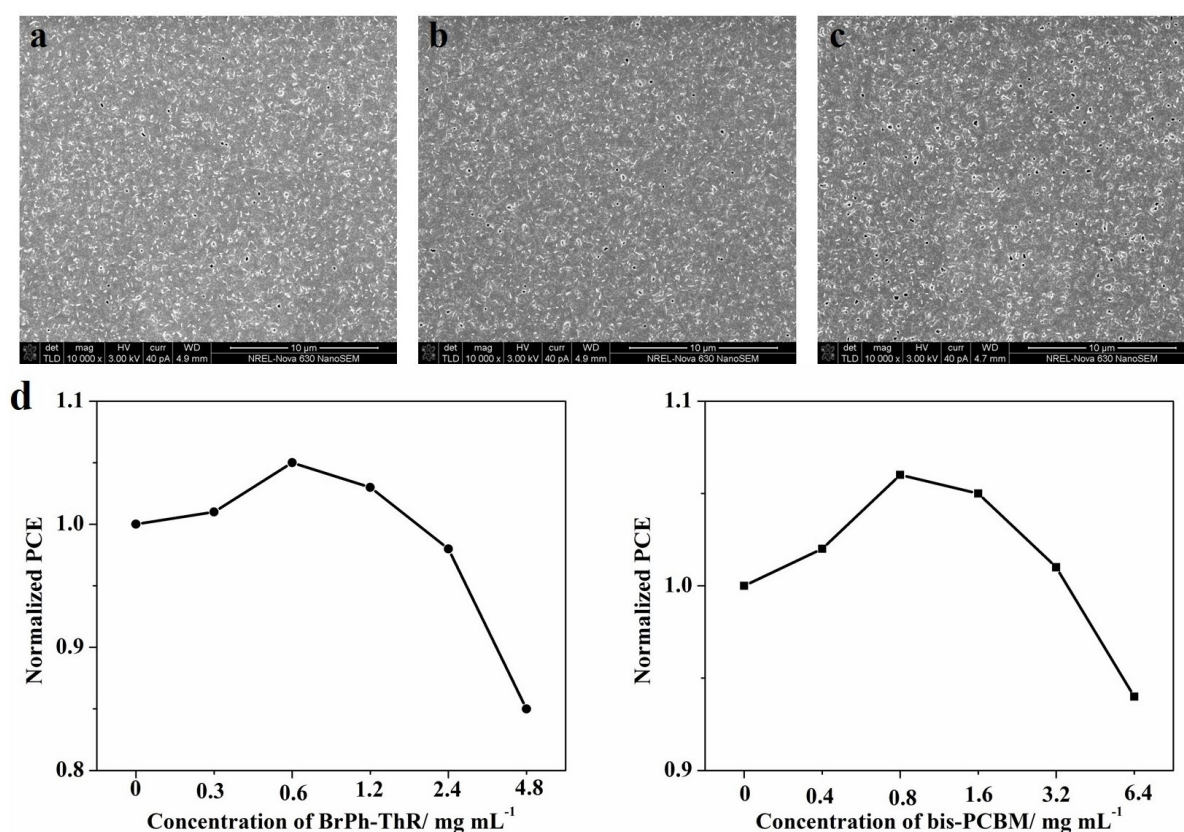


Figure S7 The surface-view SEM images of perovskite films with different amounts of BrPh-ThR. (a) 1.2 mg/mL; (b) 2.4 mg/mL; (c) 4.8 mg/mL. The scale bar is 10 μm. (d) The normalized PCE based on different concentration of BrPh-ThR- (left) and bis-PCBM- (right) containing perovskite solar cells. We first investigated the impact of different concentration of Lewis acid bis-PCBM and Lewis base BrPh-ThR on the performance and the normalized PCE was shown in **Figure S6**. A significant enhancement of performance is observed after adding a small amount of bis-PCBM in antisolvent. When the concentration of bis-PCBM is increased to 1.6 mg/mL and more, more n-type bis-PCBM will present at the perovskite/spiro-OMeTAD interface, introducing an undesired interface recombination pathway, which gives rise to the decreased performance. At a small amount of BrPh-ThR, the crystal grains of perovskite became larger and the arrangement between the grains became more dense. In addition, the perovskite thin film exhibits good uniformity, with no pinholes. However, when we further increased the amount of 2-pyridylthiourea to 4.8 mg/mL, some pinholes were present in the perovskite films (**Figure S6**), which has a negative impact on the performance. So, we choose the concentration of 0.6 mg/mL for BrPh-ThR in the perovskite precursor and 0.8 mg/mL for bis-PCBM in the antisolvent for further investigation.

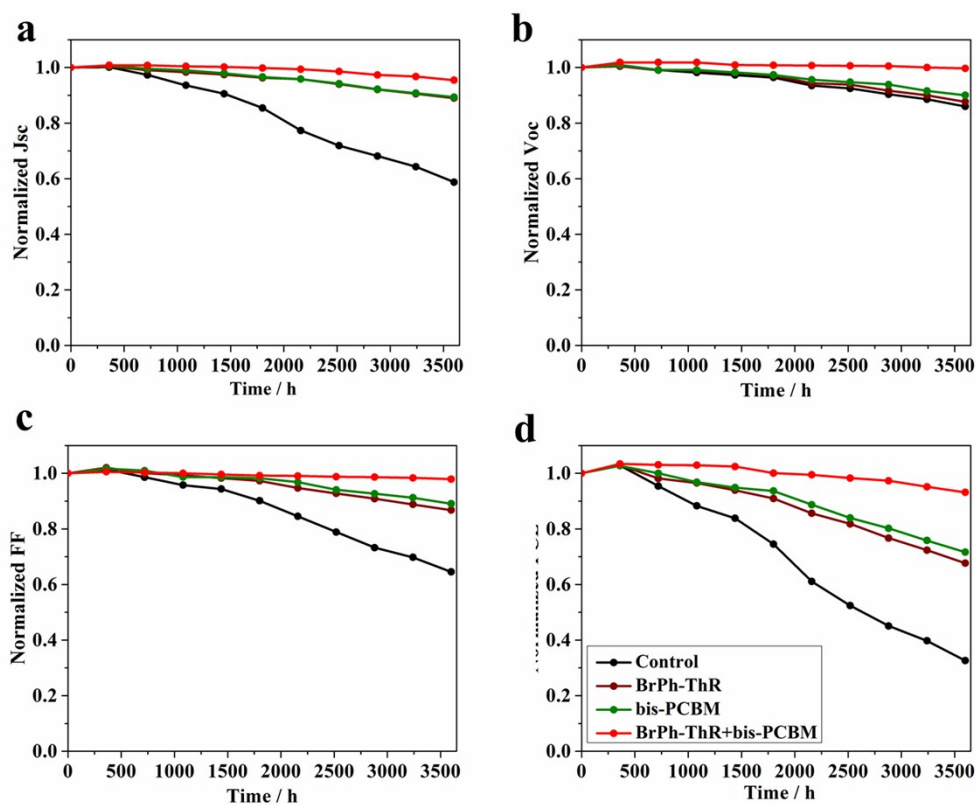


Figure S8 The stability of corresponding perovskite solar cells without any encapsulation in ambient environment of 10%–20% relative humidity.

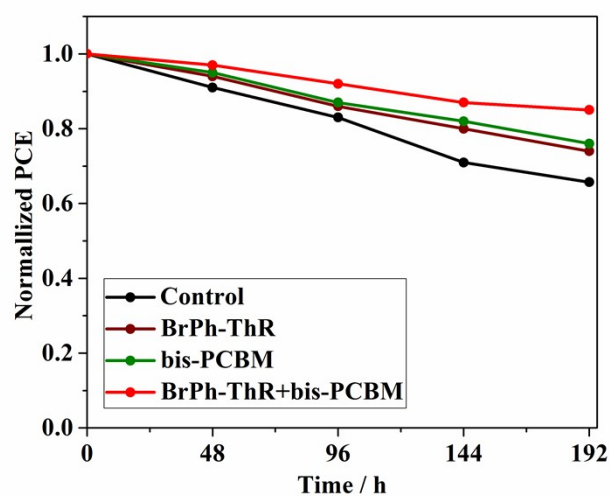


Figure S9 The stability of corresponding perovskite solar cells at 85°C in ambient environment of 10%–20% relative humidity dark storage without any encapsulation

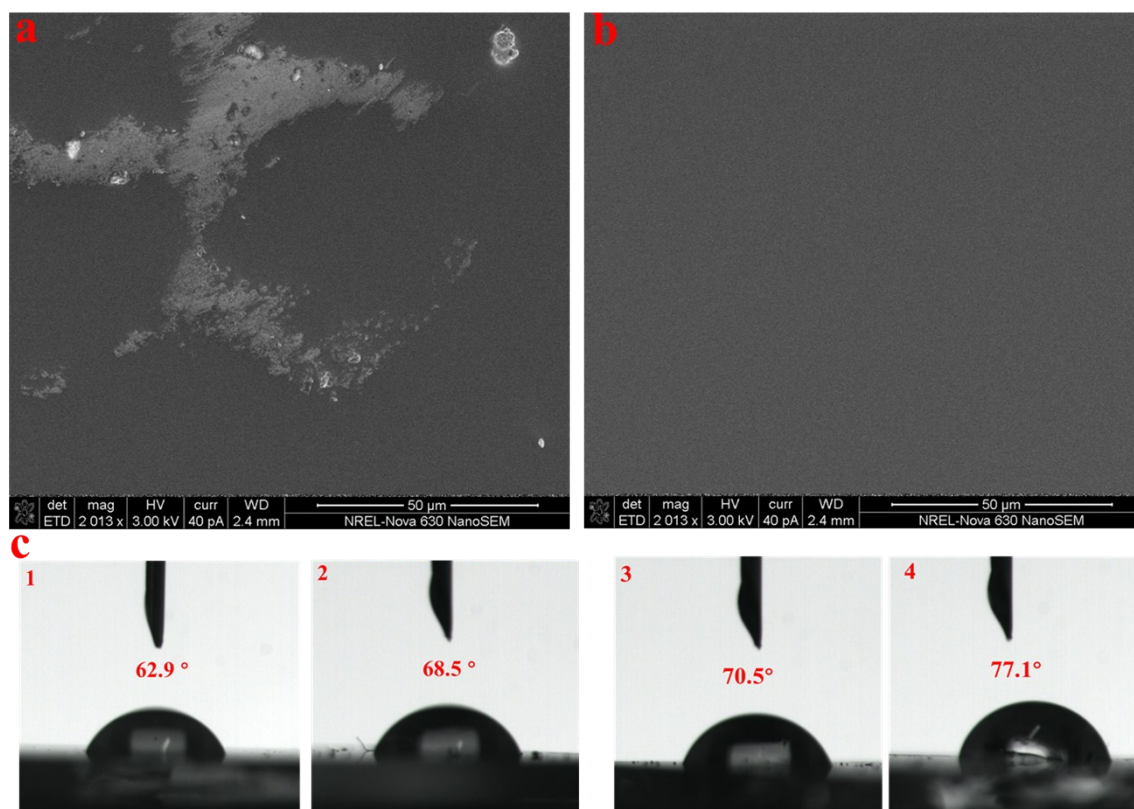


Figure S10 Surface-view SEM images of spiro-OMeTAD on (a) perovskite; (b) bis-PCBM+BrPh-ThR/perovskite. The scale bar is 50 μm. (c) The contact angles between perovskite films and chlorobenzene, **1**, BrPh-ThR + bis-PCBM; **2**, bis-PCBM; **3**, BrPh-ThR; **4**, control. The angle of the CB droplet on the BrPh-ThR + bis-PCBM-containing film was 62.9°. This can be compared with 68.5°, 70.5°, and 77.1° for bis-PCBM, BrPh-ThR, and the control, indicating better wetting of the BrPh-ThR+bis-PCBM-containing perovskite by the CB when compared with the other three samples, which is better for the film quality of HTM layer.

Table S1 Lifetimes for the first-order non-radiative carrier recombination derived from fitting the PL decay curve

Sample	$\tau = 1/k_1$ (ns)
Control	790
BrPh-ThR	1,098
Bis-PCBM	1,220
BrPh-ThR + bis-PCBM	1,526

Table S2 Performance parameters of corresponding perovskite-based solar cells under different scan directions with a bias step of 5 mV.

Sample	V_{oc} (V)	J_{sc} (mA cm ⁻²)	FF	PCE (%)
Control (backward)	1.10	23.12	0.71	18.9
Control (forward)	1.10	23.13	0.73	19.3
BrPh-ThR (backward)	1.11	23.59	0.74	20.3
BrPh-ThR (forward)	1.11	23.64	0.74	20.4
bis-PCBM (backward)	1.12	23.62	0.74	20.4
bis-PCBM (forward)	1.11	23.65	0.75	20.5
BrPh-ThR+bis-PCBM (backward)	1.13	23.88	0.77	21.6
BrPh-ThR+bis- PCBM (forward)	1.12	23.93	0.78	21.7

Table S3 The conductivity and mobility of corresponding perovskite films from the Hall effect measurement test

Sample	Conductivity (S cm ⁻¹)	Mobility (cm ² Vs ⁻¹)
Control	1.89×10 ⁻⁶	6.42
BrPh-ThR	8.96×10 ⁻⁶	29.76
bis-PCBM	9.32×10 ⁻⁶	35.67
BrPh-ThR+bis-PCBM	3.09×10 ⁻⁵	65.78